Nanosized particles in bone and dissolution insensitivity of bone mineral

Lijun Wang,[a)] George H. Nancollas,[b)] and Zachary J. Henneman
*Department of Chemistry, University at Buffalo, The State University of New York, Buffalo,
New York 14260*

Eugenia Klein[a)]
Department of Research Support, Weizmann Institute of Science, Rehovot 76100, Israel

Steve Weiner[c)]
Department of Structural Biology, Weizmann Institute of Science, Rehovot 76100, Israel

Most of the mineral crystals in bone are platelets of carbonated apatite with thicknesses of a few nanometers embedded in a collagen matrix. We report that spherical to cylindrical shaped nanosized particles are also an integral part of bone structure observed by high resolution scanning electron microscopy. High resolution back scattered electron imaging reveals that the spherical particles have a contrast similar to the crystal platelets, suggesting that they are thus likely to have similar mineral properties. By means of constant composition (CC) dissolution of bone, similar sized nanoparticles are shown to be insensitive to demineralization and are thought to be dynamically stabilized due to the absence of active pits/defects on the crystallite surfaces. Similar reproducible self-inhibited dissolution was observed with these nanoparticles during CC dissolution of synthetic carbonated apatite. This result rules out the possible influence of complicating biological factors such as the possible presence of organic matrix components and other impurities. This phenomenon can be explained by a unique dissolution model involving size considerations at the nanoscale. The unexpected presence of nanoparticles in mature bone may also be due to the stabilization of some nanosized particles during the formation process in a fluctuating biological milieux. © *2006 American Vacuum Society.* [DOI: 10.1116/1.2354575]

I. INTRODUCTION

Bone has a complex hierarchical structure from macroscopic to microscopic length scales [1–3]. The crystals in bone are plate shaped with thicknesses of 2–4 nm and have highly variable length and width dimensions (averaging 50 × 25 nm). Most are arranged in layers within a collagen matrix [4,5]. Each crystal layer is separated by four layers of collagen triple helical molecules. This nanoscale structure forms the basic composite material of bone. It is most probably responsible for much of the materials properties of bone [6].

Recent dissolution studies of synthetic hydroxyapatite and tooth enamel revealed an interesting and unusual behavior in that dissolution is effectively suppressed when crystal sizes are reduced to the nanoscale [7]. Here, we report that spherical to cylindrical shaped nanosized particles are also an integral part of mature bone structure. Similar sized particles can be dynamically stabilized under undersaturated solution conditions due to their nano-sizes, which confer remarkable characteristics of dynamic self-preservation.

II. METHODS

A. Anorganic baboon bone sample preparation

Bone samples were removed from the midshaft of the diaphysis of 2–3 years old baboons. The bone samples were stored at −20 °C prior to use. The bone structure was predominantly osteonal. The pieces were crushed in an agate mortar and pestle after freezing in liquid nitrogen. The powder was extracted with acetone and after drying it was reground. The procedure for removing the exposed organic material follows Weiner and Price [8] and briefly is as follows: the bone powder was placed in a Petrie dish and 10 ml of 5% sodium hypochlorite was added. The dish was placed on a rocking table for 2 h. The sample was then reground in the agate mortar and pestle and fresh sodium hypochlorite was added. After another 2 h the sample was transferred to a microcentrifuge tube and the sodium hypochlorite was removed by centrifugation (10 000 rpm for 2 min). The sample was washed three times with deionized water, and then twice with 100% ethanol and dried.

B. Constant composition

Dissolution experiments were made in magnetically stirred double-walled pyrex vessels. The undersaturated reaction solutions (40 mL) were prepared by mixing calcium chloride and potassium dihydrogen phosphate with sodium chloride to maintain the ionic strength, I, at 0.15 M. The pH was adjusted to the desired value, 5.50±0.01. Nitrogen, saturated with water vapor at 37 °C, was purged through the reaction solutions to exclude carbon dioxide. The dissolution reactions were initiated by the introduction of either deorganified baboon bone (3.0 mg) or carbonated (7.96%) apatite (CAP) seed crystallites (1.0 mg). Titrant addition was poten-

---
[a)]These authors contributed equally to this work.
[b)]Electronic mail: ghn@buffalo.edu
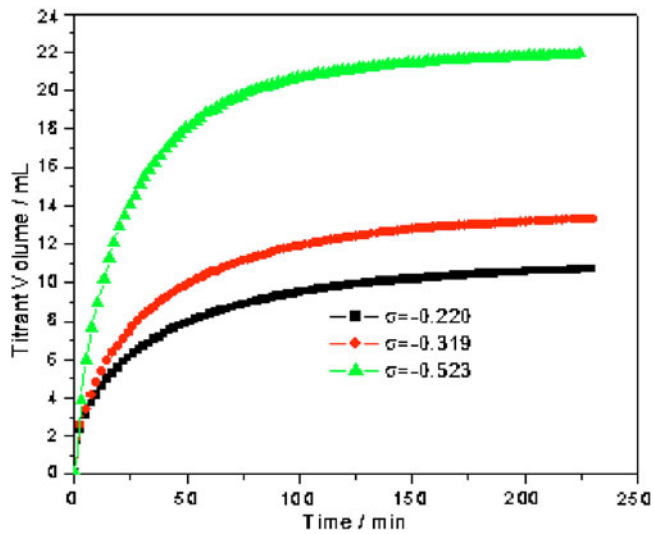[c)]Electronic mail: steve.weiner@weizmann.ac.il

FIG. 1. CC curves of titrant volume against time for baboon bone dissolution at different undersaturations. The curves have been normalized to a bone seed mass of 3.00 mg.

FIG. 2. CC curves of bone dissolution. The rates decreased virtually to zero at the end of dissolution reactions.

tiometrically controlled by glass and Ag/AgCl reference electrodes. During dissolution, the electrode potential was constantly compared with a preset value and the difference, or error signal, activated a motor-driven titrant buret. Thus a constant thermodynamic dissolution driving force was maintained. Concentrations of the titrant solutions are given by Eqs. (1)–(3),

$$T_{NaCl} = W_{NaCl} + W_{KOH} + 6C_{eff}, \tag{1}$$

$$T_{HCl} = 14C_{eff} - W_{KOH}, \tag{2}$$

$$C_{eff} = W_{Ca}/10 = W_P/6, \tag{3}$$

in which W and T are the total concentrations in the reaction solutions and titrants, respectively, and C_{eff} is the effective titrant concentration with respect to hydroxyapatite [$Ca_{10}(PO_4)_6(OH)_2$ (HAP)]. During the reactions, slurry samples were periodically withdrawn, filtered, and the solutions analyzed for calcium and phosphate. The total concentrations of calcium and phosphate remained constant to within ±1.5% during the experiments.

The dissolution flux rate, J, is calculated using Eq. (4),

$$J = \frac{C_{eff}dV}{A_T dt}, \tag{4}$$

in which dV/dt is the gradient of the constant composition (CC) titrant curves and A_T is the surface area. The initial value of A_T was calculated from the specific surface area of the seeds (110.83 m²/g for baboon bone samples and 56.55 m²/g for carbonated apatite samples), which were determined by Brunauer–Emmett–Teller nitrogen adsorption (30:70 N₂/He, Quantasorb II, Quantachrome).
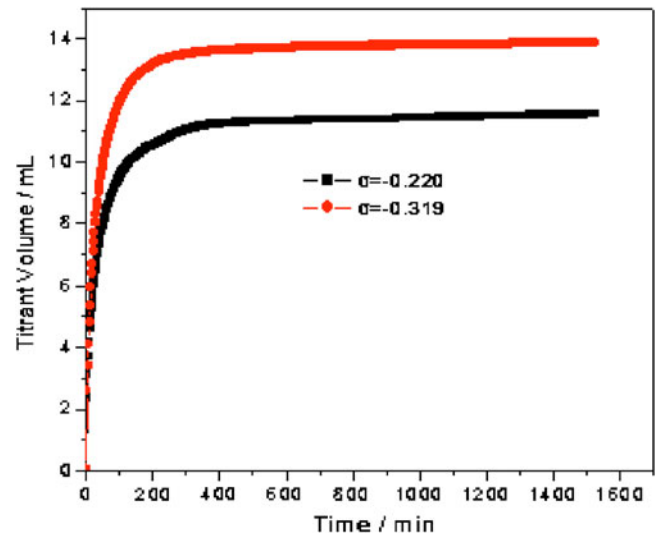
C. Undersaturation and solution speciation

The undersaturation S and relative undersaturation σ of CAP, is given by Eq. (5),

$$\sigma = S - 1 = \left[\frac{IP}{K_{sp}} \right]^{1/18} - 1, \tag{5}$$

in which, IP is ionic activity product, expressed using HAP stoichiometry. The mean value, 2.88×10^{-112} mol¹⁸ L⁻¹⁸, was used as K_{sp} in this dissolution study. This was further confirmed by the direct CC dissolution/growth experiments in which the values of the relative supersaturation were maintained in the presence of CAP seed at 0.00±0.07 for periods of about 8 h to determine the conditions corresponding to zero reaction rate. The value of K_{sp} may be compared with that of pure HAP, 5.52×10^{-118} mol¹⁸ L⁻¹⁸.[9] The solution is undersaturated when $\sigma < 0$. Solution speciation calculations were made by using the extended Debye–Hückel equation proposed by Davies from mass-balance expressions for total calcium and total phosphate with appropriate equilibrium constants by successive approximation for the ionic strength.

D. Scanning electron microscopy

1. Anorganic bone powder

The dry bone powder was resuspended in a small amount of 100% ethanol, and a drop was placed on a carbon coated transmission electron microscopy (TEM) copper grid and blotted. This was then stuck on 0.7 mm deep wells to an aluminum scanning electron microscopy (SEM) stub using tiny springs. The samples were examined uncoated in a Zeiss Ultra SEM at very short working distances (2 mm) and low voltages (from 3 kV landing voltages for the coated samples, to 0.7 for the uncoated) and fast scanning times to avoid charging or after a freshly applied coating of a 2 nm thick layer of chromium (coating current 100 mA in an Emitech
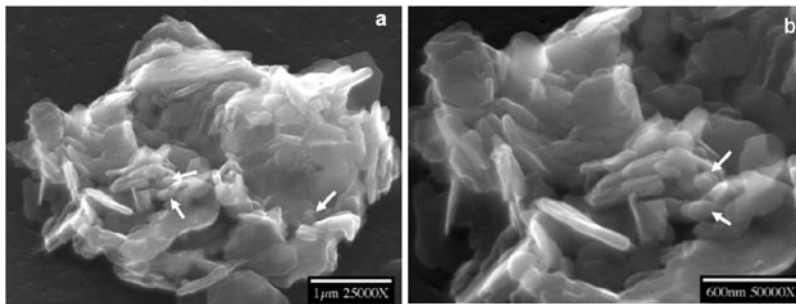
FIG. 3. SEM images of partially demineralized baboon bone at $\sigma=-0.220$ (a) and $\sigma=-0.319$ (b) after a shorter dissolution period (less than 1 h). Nanosized particles about $20-100$ nm (shown by arrows) and the typical plate-like crystals can be seen at both undersaturations.

k575X sputter). Two signals were detected for high resolution pictures: (1) The low energy secondary electrons with energies from 0 to 0.7 eV were detected by the InLens secondary electrons detector. (2) The slightly higher energy backscattered electrons, filtered by the ESB bias set to 400 V, that admits the backscattered electrons with energies between 400 and 700 eV. These were detected by the ESB detector.

2. Dissolution residues

Crystallites were collected from the bulk solution by filtration (Polycarbonate membrane filters, 0.05 μm pore size, SterliTech), both during and at the end of the dissolution experiments, and were dried at room temperature. Samples, under vacuum, were sputter coated with a thin carbon deposit to provide conductivity, and then examined using a field-emission SEM (Hitachi S-4000), typically at 20 keV.

III. RESULTS AND DISCUSSION

Under physiological conditions of temperature (37 °C) and ionic strength (0.15 M), the demineralization of anorganic baboon osteonal bone has been investigated at relative undersaturations ranging from −0.220 to −0.523 at pH 5.50. Typical titrant-time curves using a nanomolar-sensitive CC technique,[10] shown in Fig. 1, reached plateaus over an extended experimental period prior to complete dissolution (Fig. 2). This indicates the formation of metastable states in which the reaction was effectively suppressed even though the reaction solutions remained undersaturated. Some of the nanosized particles (20–100 nm) can be seen at undersaturations of both $\sigma=-0.220$ [Fig. 3(a)] and $\sigma=-0.319$ [Fig. 3(b)] after relatively short dissolution periods (<1 h). However, further dissolution of these nanosized particles (>1 d) was suppressed. There are two possible sources for these nanoparticles: (1) They may be present in the initial bone structure and are not products of dissolution or (2) they are formed as a result of the dissolution of the platelet crystals. It is also conceivable that both sources exist.

High resolution SEM images of anorganic fractured baboon bone showed that spherical to cylindrically shaped particles, approximately 20 nm in diameter, are present (Fig. 4). They are clearly an integral part of the layered structure of bone. Similar spherical particles were observed on the fracture surfaces of untreated bone, but due to the presence of collagen, we could not distinguish between particles derived

from the collagenous matrix and mineral particles. We also observed these particles on uncoated anorganic bone specimens thereby excluding the possibility that they were coating artifacts (Fig. 5). A comparison of the same bone particles using secondary electrons and the BSE is shown in Fig. 6. The secondary electron image [Fig. 6(a)] shows the particle topography, whereas the backscattered electron image [Fig. 6(b)] reflects the particle atomic density. In the high resolution backscattered electron image the spherical particles have a contrast similar to the crystal platelets. They are thus likely to have similar mineral properties.

It is unfortunately difficult to acquire independent evidence to support the tentative conclusion that the particles and the plate-shaped crystals have similar mineral properties. Application of TEM to obtain electron diffraction patterns of these spherical particles may not be possible due to sample preparation difficulties. We attempted to observe bone powders directly under the TEM, but it is difficult to identify the rounded particles because of projection problems and the associated plate-shaped particles contribute to the diffraction patterns. Using a focused ion beam in the dual beam SEM to prepare thin sections is also problematic, because the high energy ion beam may change the mineral crystallite phases during sample preparation. Hassenkam *et al.* used atomic force microscopy (AFM) to image the exterior surface of intact and fractured trabecular bone and found small
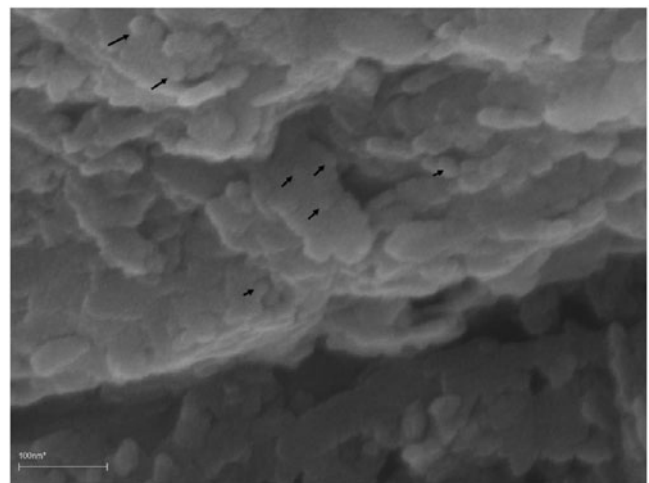

FIG. 4. High resolution SEM image of spherical to cylindrically shaped particles shown by arrows around 20 nm in diameter on fractured surfaces of coated baboon bone sample prior to dissolution.
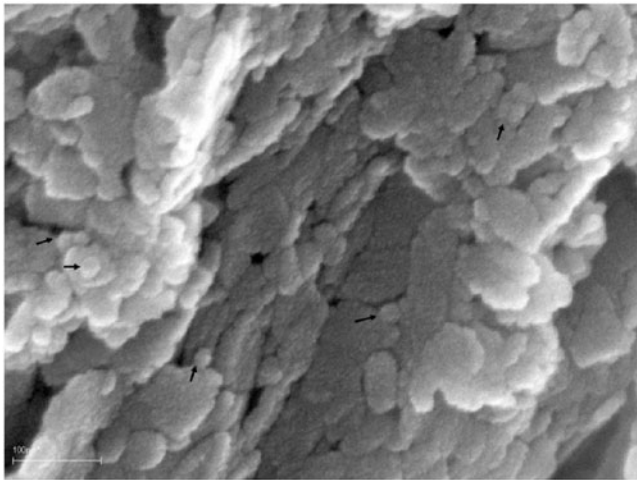
FIG. 5. High resolution SEM image of uncoated baboon bone sample prior to dissolution. Samilar nanosized particles are indicated by arrows.

20–30 nm nodular structures between collagen fibrils and a dense array of mineral plates.[11] However, even the plate-shaped crystals tended to have a rounded appearance because of the operation mode of the AFM. We are therefore limited to the high resolution BSE imaging technique that, at this point, provides the most informative information on the mineral properties of the nanoparticles.

Nanoparticles from baboon bone were released directly into the solution by fluid diffusion flux and were stabilized against dissolution in the bulk solution [Figs. 7(a) and 7(b)]. In situ energy dispersive spectra (EDS) indicate that these residual crystallites were composed of apatitic phases similar to those prior to demineralization [Fig. 7(c)]. The apatitic residues of the demineralization reactions are stabilized against further dissolution in the undersaturated aqueous solution. We have no evidence that these particles are the same as those observed in intact bone.

Since bone contains significant amounts (3%–8%) of carbonate,[12,13] the CAPs may serve as more suitable biomineral models than pure HAP. To exclude the influence of possible organic residues in the bone dissolution experiments, CC dissolution studies were also made using granular synthetic carbonated apatite samples [Fig. 8(b)] of high purity (>99.4%) containing 7.96% carbonate. At a relatively high undersaturation ($\sigma = -0.319$), these CAPs undergo rapid dissolution and most of solid phase is dissolved in less than 4 h. The CC dissolution curves reach plateaux prior to complete dissolution at both undersaturations [Fig. 8(a)], thus indicating the creation of metastable states in which the reaction is effectively terminated even though the CAP crystallites remain in contact with undersaturated solutions. Similar nanosized crystallites residues were observed at the end of these dissolution reactions [Figs. 8(c) and 8(d)]. At two experimental undersaturations of −0.220 and −0319, less than 50% of the CAP crystallites undergo dissolution before the reaction is effectively stopped or the rate is reduced to a very low value. These observations are similar to those made during bone demineralization.
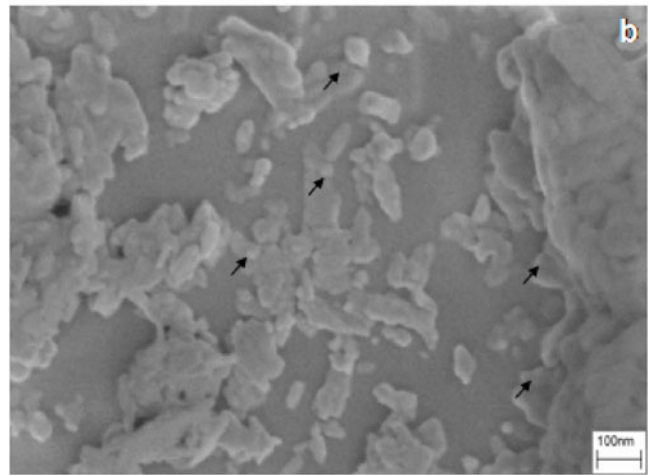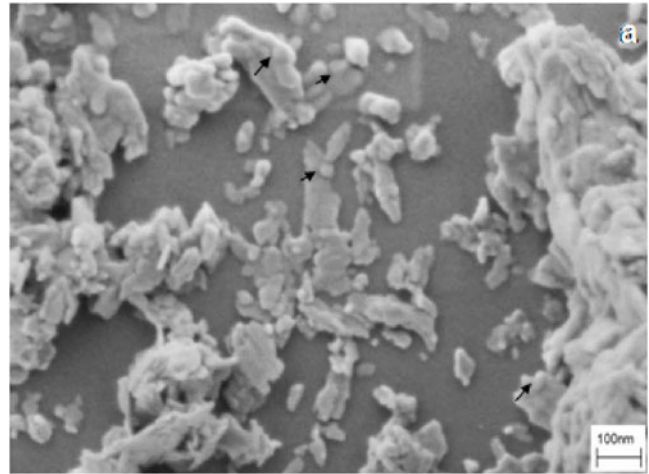

FIG. 6. High resolution images of bone particles (shown by arrows) using (a) the secondary electron detector and (b) the backscattered electron detector. The secondary electron detector shows changes in topography, whereas the backscattered electron detector shows changes in atomic density.

It is well known that the dissolution of crystals is highly dependent on the thermodynamic driving forces, usually expressed in terms of the relative undersaturation, σ. Hitherto it was considered that when $\sigma < 0$, all crystals would inexorably dissolve until all the solid phases had disappeared. The demonstrated importance of pit formation during dissolution has markedly changed our understanding of this process.[14] Demineralization of sparingly soluble salts such as the apatites is generally initiated and accompanied by the formation and development of pits on the crystal surfaces, and the dissolution rates are also determined by pit densities and spreading velocities.[15,16] Recent CC dissolution studies of synthetic HAP have confirmed this interesting and unusual behavior in that dissolution rates decreased, eventually resulting in effective suppression, when their sizes fell into a critical length scale—always at the nanoscale.[17] Lasaga and Lüttge have also used vertical scanning interferometry during dissolution, Monte Carlo simulations of etch pit formation, and empirical bulk dissolution rates to derive a dissolution rate law that is consistent with data for several minerals. This rate law predicts that the slower rates of dissolution
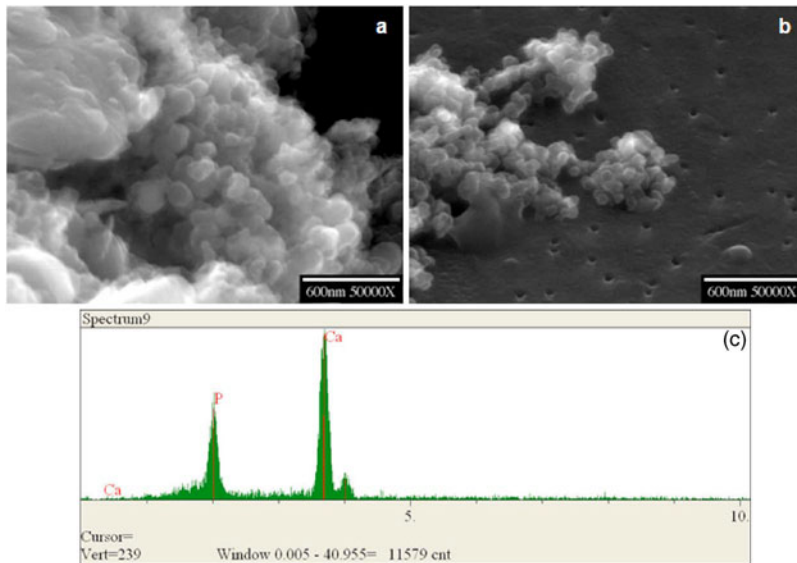
FIG. 7. SEM images of nanosized particles collected from the bulk solution at $\sigma=-0.220$ (a) and $\sigma=-0.319$ (b) by filtration at the end of dissolution experiments; (c) EDS of nanoparticles, showing residual crystallites were apatitic phases similar to those prior to demineralization.

measured in the field arise from metastable phases that hinder the reactions and that the process is nonlinear even as equilibrium conditions are approached.[18]

Clearly, this dissolution termination is a kinetic phenomenon and it can be explained in terms of a dissolution model that incorporates particle size considerations. Analogous to the formation of two dimensional nuclei/hillocks for crystal growth, in dissolution the rate of step movement from a pit of radius r can be obtained from treatments similar to the model of Burton, Cabrera, and Frank for the corresponding crystal growth processes[19,20]

$$R(r) = R_\infty \left[1 - \frac{e^{(1-S)r^*/r} - 1}{e^{1-S} - 1} \right] \approx R_\infty \left(1 - \frac{r^*}{r} \right), \quad (6)$$

where r^*, the critical radius for the formation of a two-dimensional pit/dissolution step, is given by Eq. (7),

$$r^* = \frac{\gamma_{SL}\Omega}{|\Delta g|} \text{ and } \Delta g = kT \ln S. \quad (7)$$

In Eq. (7), γ_{SL} is interfacial tension, k is the Boltzmann constant, Ω is the area occupied by each dissolution unit and Δg,
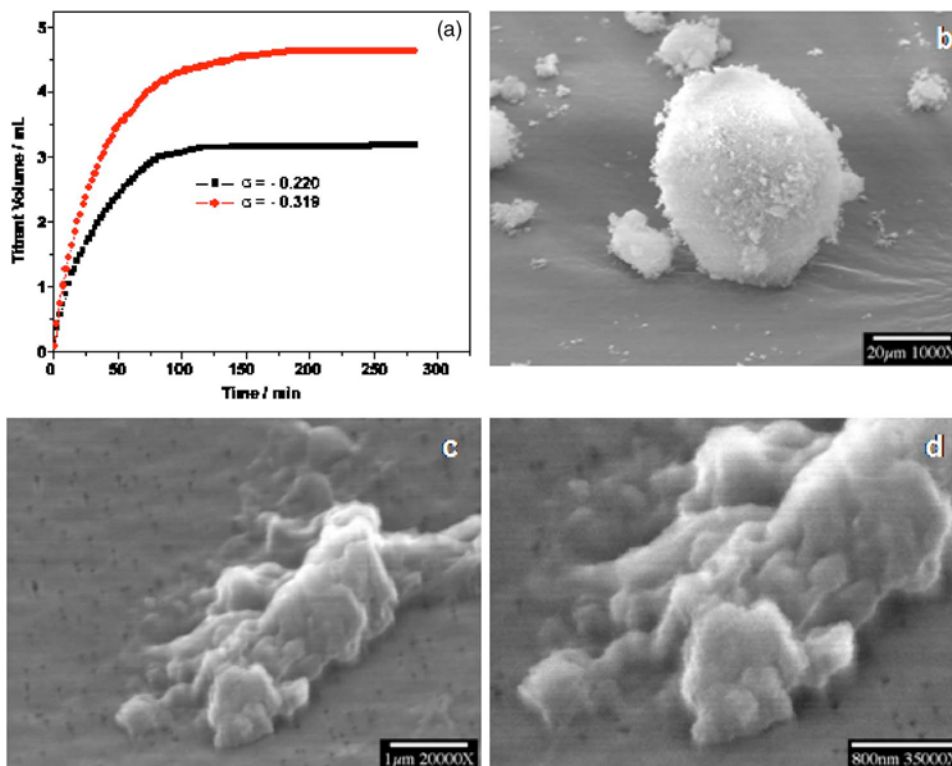

FIG. 8. CC dissolution of synthetic carbonated apatite. (a) CC plots of titrant volume against time at different undersaturations. SEM images of synthetic carbonated apatite before dissolution (b) and after dissolution (c). Similar nanosized crystallite residues are observed at the dissolution suppressed stage at $\sigma=-0.319$ (d). The results are similar to those for baboon bone dissolution.

the Gibbs free energy change for dissolution. In Eq. (6), R_∞ is the velocity of dissolution steps at $r \rightarrow \infty$. It has been shown that only pits which are larger than r^* provide the active dissolution sites that contribute to dissolution. When r is closer to r^*, there is no fast movement of its stepwave and the dissolution rate approaches zero [Eq. (6)]. The critical size of pits, r^*, is a function of undersaturation [Eq. (7)]. When the dimensions of the crystallites (l) are of the same order as r^* during the dissolution (e.g., l becomes less than $20\ r^*$), the formation of active pits is more difficult since their sizes are restricted to those of the small crystallites. As shown by Eq. (6), $R(r)$ is strongly dependent on pit size. Correspondingly, the macroscopic CC dissolution rate decreases with the extent of dissolution [Figs. 2 and Fig. 8(a)]. Residues of these nanoparticles at the end of dissolution reactions or preexisting nanoparticles that are stabilized due to the lack of surface defects/pits are able to resist dissolution. The phenomena of dissolution termination and "critical" pit size are not arbitrary; rather, these self-tuned and dissolution-insensitive effects for tiny crystallites and biomaterials such as tooth enamel[21,22] occur specifically at the nanoscale. In addition, since traditional solution theories are based on experiments involving soluble salts, these phenomena are not observed since the critical conditions would be outside the range of the experimental techniques employed.

We do not know whether the nanosized particles present in bone are the same as those that are insensitive to dissolution. It is, however, conceivable that the existence of both phenomena can be attributed to the same basic mechanism of formation, namely that a certain proportion of particles of nanoscale dimensions have defect free surfaces and are thus stabilized during formation of bone or dissolution of bone. Their presence in bone and their formation during dissolution may, however, have important implications to the dual functions of bone, namely during load bearing and as a reservoir for mineral ions needed for metabolism. Gao *et al.* have suggested that the size of the mineral particles—typically tens to hundreds of nanometers, is not arbitrary.[6] Rather, it seems to give biominerals such as bone and tooth remarkable characteristics: as the mineral size falls below a critical length scale (around 20–50 nm), (a) the strength of a perfect mineral crystal is maintained and (b) the biomaterials become insensitive to dissolution at the nanoscale.

In this article, we use two independent observational methods to study the stabilization of particles in bone at the nanoscale. The results provide important insights into the nanostructured architecture of a complex biocomposite. These nanosized particles in bone will be expected to show a remarkable degree of self-preservation in the fluctuating physiological milieu, and, in association with organic matrix, may be related to the growth conditions in which some particles remain stable at a critical size, whereas most particles continue to grow into platelets.

ACKNOWLEDGMENTS

[1] J. Y. Rho, L. Kuhn-Spearing, and P. Zioupos, Med. Eng. Phys. **20**, 92 (1998).

[2] S. Weiner and H. D. Wagner, Annu. Rev. Mater. Sci. **28**, 271 (1998).

[3] W. J. Landis, Bone (N.Y.) **16**, 533 (1995).

[4] W. J. Landis and K. J. Hodgens, J. Struct. Biol. **117**, 24 (1996).

[5] P. Roschger, B. M. Grabner, S. Rinnerthaler, W. Tesch, M. Kneissel, A. Berzlanovich, K. Klaushofer, and P. Fratzl, J. Struct. Biol. **136**, 126 (2001).

[6] H. Gao, B. Ji, L. J. Ingomar, E. Arz, and P. Fratzl, Proc. Natl. Acad. Sci. U.S.A. **100**, 5597 (2003).

[7] R. K. Tang, L. J. Wang, C. A. Orme, T. Bonstein, P. J. Bush, and G. H. Nancollas, Angew. Chem., Int. Ed. **43**, 2697 (2004).

[8] S. Weiner and P. A. Price, Calcif. Tissue Int. **39**, 365 (1986).

[9] L. J. Shyu, L. Perez, S. J. Zawacki, J. C. Heughebaert, and G. H. Nancollas, J. Dent. Res. **62**, 398 (1982).

[10] M. B. Tomson and G. H. Nancollas, Science **200**, 1059 (1978).

[11] T. Hassenkam, G. E. Fantner, J. A. Cutroni, J. C. Weaver, D. E. Morse, and P. K. Hansma, Bone (N.Y.) **35**, 4 (2004).

[12] R. Z. LeGeros and M. S. Tung, Caries Res. **17**, 419 (1983).

[13] A. A. Baig *et al.*, Calcif. Tissue Int. **64**, 437 (1999).

[14] *Kinetic Theory in Earth Sciences*, Princeton Series in Geochemistry, edited by A. C. Lasaga (Princeton University Press, Princeton, NJ, 1998).

[15] A. Lüttge, J. Electron Spectrosc. Relat. Phenom. **150**, 248 (2006).

[16] P. M. Dove, N. Han, and J. J. De Yoreo, Proc. Natl. Acad. Sci. U.S.A. **102**, 15357 (2005).

[17] R. K. Tang, G. H. Nancollas, and C. A. Orme, J. Am. Chem. Soc. **123**, 5437 (2001).

[18] A. C. Lasaga and A. Lüttge, Science **291**, 2400 (2001).

[19] W. K. Burton, N. Cabrera, and F. C. Frank, Philos. Trans. R. Soc. London, Ser. A **243**, 299 (1951).

[20] R. K. Tang, C. A. Orme, and G. H. Nancollas, J. Phys. Chem. B **107**, 10653 (2003).

[21] L. J. Wang, R. K. Tang, T. Bonstein, C. A. Orme, P. J. Bush, and G. H. Nancollas, J. Phys. Chem. B **109**, 999 (2005).

[22] L. J. Wang, R. K. Tang, T. Bonstein, P. J. Bush, and G. H. Nancollas, J. Dent. Res. **85**, 359 (2006).